Research Square

Preprints are preliminary reports that have not undergone peer review.
They should not be considered conclusive, used to inform clinical practice,
or referenced by the media as validated information.

Pre-monsoon heatwave trends and ENSO-dryness associations in Rajshahi, Bangladesh

Fahim Shahriar Pranto

pfahimshahriar@gmail.com

University of Dhaka

Abdullah Osama Swaccho

Aston University

Research Article

Keywords: Heatwave, ENSO, Soil moisture, Negative Binomial regression, Hindcast verification, Bangladesh

Posted Date: November 13th, 2026

DOI: https://doi.org/10.21203/rs.3.rs-11397313/v1

License: This work is licensed under a Creative Commons Attribution 4.0 International License.
Read Full License

Additional Declarations: No competing interests reported.

Pre-monsoon heatwave trends and ENSO-dryness associations in Rajshahi, Bangladesh

Fahim Shahriar Pranto[1] · Abdullah Osama Swaccho[2]

[1] Institute of Disaster Management and Vulnerability Studies, University of Dhaka, Dhaka 1000, Bangladesh

[2] School of Engineering and Technology, Aston University, Birmingham B4 7ET, United Kingdom

Corresponding author: Fahim Shahriar Pranto, e-mail: pfahimshahriar@gmail.com

Acknowledgements

The authors thank the Bangladesh Meteorological Department (BMD) for providing surface meteorological observation records for Rajshahi station. We acknowledge the European Centre for Medium-Range Weather Forecasts (ECMWF) Copernicus Climate Change Service for the ERA5 and ERA5-Land reanalysis datasets, the NOAA Physical Sciences Laboratory for ERSSTv5 sea surface temperature products, and the Climate Hazards Center at the University of California, Santa Barbara, for CHIRPS precipitation data.

Abstract

Pre-monsoon (March-May) heat extremes in the Barind Tract of northwestern Bangladesh threaten agriculture, water resources and public health. Using a 36-year record (1990-2025) from the Bangladesh Meteorological Department (BMD) station at Rajshahi, with satellite precipitation and ERA5/ERA5-Land reanalysis, this study assesses heatwave trends, hydroclimatic associations, circulation context and out-of-sample predictability. A heatwave day lies within a spell of at least two consecutive days with maximum temperature ≥ 36.0 °C. Rajshahi averaged 31.0 ± 12.4 heatwave days per season (range 4-52). Heatwave days increased by +4.8 days per decade (95% confidence interval [CI] 1.8-7.8; $p = 0.008$; false discovery rate [FDR] $q = 0.016$), whereas the trend in seasonal peak temperature (+0.28 °C per decade) was not significant after FDR control ($q = 0.056$). Antecedent January-March root-zone (0-28 cm) soil moisture was inversely associated with heatwave days (Spearman's $\rho = -0.364$; $p = 0.029$), but preceding-August El Niño-Southern Oscillation (ENSO) anomalies in the Niño 3.4 region were not ($\rho = 0.095$; $p = 0.58$). An intercept-only Negative Binomial climatology had the lowest corrected Akaike Information Criterion, and rolling-origin hindcasts (2005-2025) produced negative Brier Skill Scores, indicating no skill beyond climatology. Severe seasons coincided with mid-tropospheric anticyclonic ridging, rainfall deficits and enhanced sensible heat flux. Because hindcast skill was absent, a 2027 El Niño-dryness scenario (mean 34.0 heatwave days; 95% prediction interval 14-60) is presented as a model-conditioned stress test, not a forecast. The pre-specified verification protocol offers a replicable standard for transparent heat-hazard assessment in data-sparse regions.

Keywords: Heatwave, ENSO, Soil moisture, Negative Binomial regression, Hindcast verification, Bangladesh

1 Introduction

1.1 Pre-monsoon heat extremes in northwestern Bangladesh

Surface air temperature extremes during the pre-monsoon transition season (March to May; MAM) pose severe environmental, physiological, and socioeconomic challenges across the Bengal Basin. Situated within the elevated Barind Tract of northwestern Bangladesh, the Rajshahi district experiences some of the most intense thermal regimes in South Asia (Bangladesh Meteorological Department [BMD] 2019). During late spring, daily maximum temperatures frequently exceed 36.0 °C and regularly surpass 40.0 °C, generating prolonged periods of thermal stress that intersect with vital agricultural operations, notably the manual

harvesting of the irrigated winter rice crop (Boro rice). In this densely populated agrarian landscape, outdoor manual laborers face substantial occupational heat exposure, contributing to elevated risks of heat exhaustion, dehydration, and acute medical emergencies.

In addition to public health consequences, severe pre-monsoon heatwaves exert profound pressures on regional environmental systems. Sustained high temperatures accelerate surface evapotranspiration, rapidly deplete shallow soil moisture, and intensify agricultural water demand. Because the Barind Tract relies heavily on groundwater abstraction for dry-season irrigation, prolonged thermal spells exacerbate water-table drawdowns and strain local rural electricity distribution networks burdened by continuous irrigation pumping and residential cooling demands. Understanding the historical behavior and physical dynamics of heat extremes in this region is therefore critical for sustainable water management and agricultural resilience.

Long-term assessment of regional heat extremes requires consistent empirical definition criteria. Historically, climate assessments in South Asia have often relied on isolated single-day temperature thresholds or discontinuous regional observations. However, sustained multi-day heat spells impose distinct cumulative physiological and ecological burdens compared with transient single-day extremes. In recognition of these differences, BMD has operationalized a hierarchical classification that distinguishes isolated hot days from continuous multi-day events (BMD 2019). Applying these operational criteria systematically across continuous meteorological station records allows researchers to establish baseline climatologies and quantify multidecadal changes in prolonged thermal hazard.

The Barind Tract presents distinct microclimatic and edaphic features that heighten its sensitivity to atmospheric heating. The region is characterized by Pleistocene clay terraces with reduced infiltration capacity and low organic matter content, which facilitate rapid surface desiccation following periods of low rainfall. Unlike the surrounding lowlands that benefit from extensive perennial river networks and persistent wetlands, the elevated topography of the Barind Tract limits natural surface water retention. Consequently, the regional land surface warms rapidly in early spring as solar insolation intensifies, creating localized thermodynamic conditions that favor strong sensible heat transfer to the lower troposphere.

The observational infrastructure maintained by BMD across the western administrative divisions reflects an operational commitment to standardized surface synoptic monitoring. The Rajshahi station operates under national meteorological observation manuals aligned with

regional World Meteorological Organization (WMO) Regional Association II (Asia) standards. Daily observations are recorded by trained meteorological personnel at synoptic intervals, with maximum thermometers read and reset according to standard diurnal schedules. Station metadata and quality-control procedures were assessed to evaluate observational continuity and internal consistency over the study period.

Socioeconomic vulnerability in Rajshahi further amplifies the hazard posed by intense heatwaves. The district supports an intensive cropping regime centered on double- and triple-cropped rice and seasonal vegetable production. Peak harvesting activities require farm workers to spend consecutive hours in unshaded agricultural fields during the warmest hours of the day. The absence of localized cooling shelters and limited access to public hydrologic infrastructure create substantial barriers to personal heat adaptation, rendering the rural populace susceptible to cumulative thermal fatigue over extended multi-day heat episodes.

1.2 Enso, soil moisture and heatwave variability

Interannual fluctuations in South Asian climate extremes are governed by the interplay between large-scale ocean-atmosphere teleconnections and regional land-atmosphere boundary feedback. Among broad-scale oceanic drivers, the El Niño-Southern Oscillation (ENSO) is recognized as a dominant mode of tropical climate variability (Webster et al. 1998; Kumar et al. 2006). During the developing and mature phases of El Niño, positive sea-surface temperature (SST) anomalies across the central and eastern equatorial Pacific disrupt the tropical Walker circulation. This disruption typically induces anomalous large-scale subsidence and anticyclonic flow over northern India and the northern Bay of Bengal (Huang et al. 2017). Such synoptic configurations tend to suppress regional convective cloud development, enhance incoming shortwave solar radiation, and reduce pre-monsoon precipitation accumulations (Funk et al. 2015).

Simultaneously, antecedent terrestrial boundary conditions exert a critical regulatory control over surface climate in transitional hydrologic regimes (Seneviratne et al. 2010). In regions where evapotranspiration is constrained by available soil water rather than net radiation, deficits in root-zone soil moisture fundamentally alter surface energy partitioning. Following dry winter and early spring conditions, the depletion of moisture in the active vegetative rooting depth severely curtails latent heat flux (evaporative cooling). As a consequence, available surface net radiation is channeled into sensible heat flux, which accelerates the warming of the

atmospheric boundary layer and creates positive thermodynamic feedback (Miralles et al. 2014).

In the Barind Tract of Bangladesh, late winter (January to February) and early spring (March) are climatologically characterized by low precipitation accumulations. Consequently, the status of 0-28 cm root-zone soil moisture prior to the onset of the pre-monsoon peak heating window represents a potential preconditioning mechanism. When dry antecedent soil conditions coincide with favorable large-scale atmospheric circulation anomalies, regional surface heating may be substantially reinforced. However, the degree to which antecedent land-surface dryness and oceanic SST anomalies provide independent or interactive statistical explanatory power for local heatwave frequency remains an open empirical question.

The coupling between land-surface hydrology and atmospheric heating is particularly acute during the pre-monsoon months because the regional atmospheric boundary layer is relatively dry prior to the arrival of the southwest monsoon. During March and April, northwesterly continental air masses frequently advect dry, warm air from northern India into western Bangladesh. If the local land surface is already depleted of moisture, there is minimal local evaporative buffering to temper this continental advection. Conversely, when winter rains provide adequate soil moisture storage, early-season evapotranspiration can sustain higher latent heat fluxes, dampening near-surface temperature escalation.

Despite these recognized physical processes, the operational predictability of South Asian heat extremes remains constrained by high internal atmospheric variability. While coupled ocean-atmosphere models capture broad equatorial SST anomalies with multi-month lead times, resolving the precise regional manifestation of mid-tropospheric anticyclonic anomalies over the Bengal Basin involves substantial stochastic uncertainty. Evaluating whether seasonal statistical models based on antecedent teleconnection indices can provide genuine predictive skill beyond reference climatology is therefore essential for realistic climate service development.

1.3 Research gap and objectives

Despite growing scientific interest in compound climate extremes, three critical methodological and empirical gaps persist in the literature regarding Bangladesh heat extremes. First, multidecadal assessments based on continuous in-situ daily meteorological records remain limited. Few studies have applied standardized multi-day event tracking algorithms that formally separate single-day exceedances from persistent heatwave runs while applying false

discovery rate corrections across multiple trend hypotheses. Second, while oceanic teleconnections and soil moisture have each been studied in isolation, their joint empirical behavior, potential multiplicative interactions, and relative predictive contributions have rarely been evaluated within a formal, information-theoretic model selection ladder. Third, prospective climate studies in developing regions frequently present statistical regression outputs as operational seasonal forecasts without transparent out-of-sample hindcast verification, creating an unverified expectation of seasonal predictive skill.

The Rajshahi BMD station constitutes the most data-continuous meteorological record within the broader Barind Tract agroclimatic zone, which extends across Chapai Nawabganj, Naogaon, and Bogra districts in Bangladesh and into the Malda and Murshidabad districts of West Bengal, India. While existing regional temperature analyses from this Indo-Gangetic corridor indicate above-average pre-monsoon warming rates broadly consistent with South Asian trends (BMD 2019; Nissan et al. 2019), station-specific multi-decade heatwave climatologies combining continuous event-tracking, teleconnection evaluation, and prospectively verified forecast skill assessments remain absent for northwestern Bangladesh. Establishing a rigorously verified baseline at Rajshahi therefore provides a replicable methodological framework applicable to climate service agencies across the eastern Indo-Gangetic Plain and to Heat Action Plan development for districts throughout Rajshahi division.

To address these issues, the present study investigates pre-monsoon heatwaves in Rajshahi across 36 consecutive years (1990-2025). The research is structured around four primary objectives: (1) Establish a 36-year climatology and assess multidecadal trends and potential changepoints in pre-monsoon heatwave metrics using BMD daily maximum temperature observations; (2) Evaluate empirical associations between heatwave frequency, antecedent ENSO phases, and 0-28 cm root-zone soil moisture using a pre-specified Negative Binomial generalized linear model ladder; (3) Examine composite synoptic atmospheric circulation and surface turbulent energy balance anomalies to provide descriptive physical context for extreme heatwave seasons; and (4) conduct a rolling-origin out-of-sample hindcast validation (2005-2025) to benchmark forecast capability against reference climatology, followed by a model-conditioned 2027 ENSO-dryness stress test evaluating system sensitivity under adverse boundary conditions (Fig. 1).

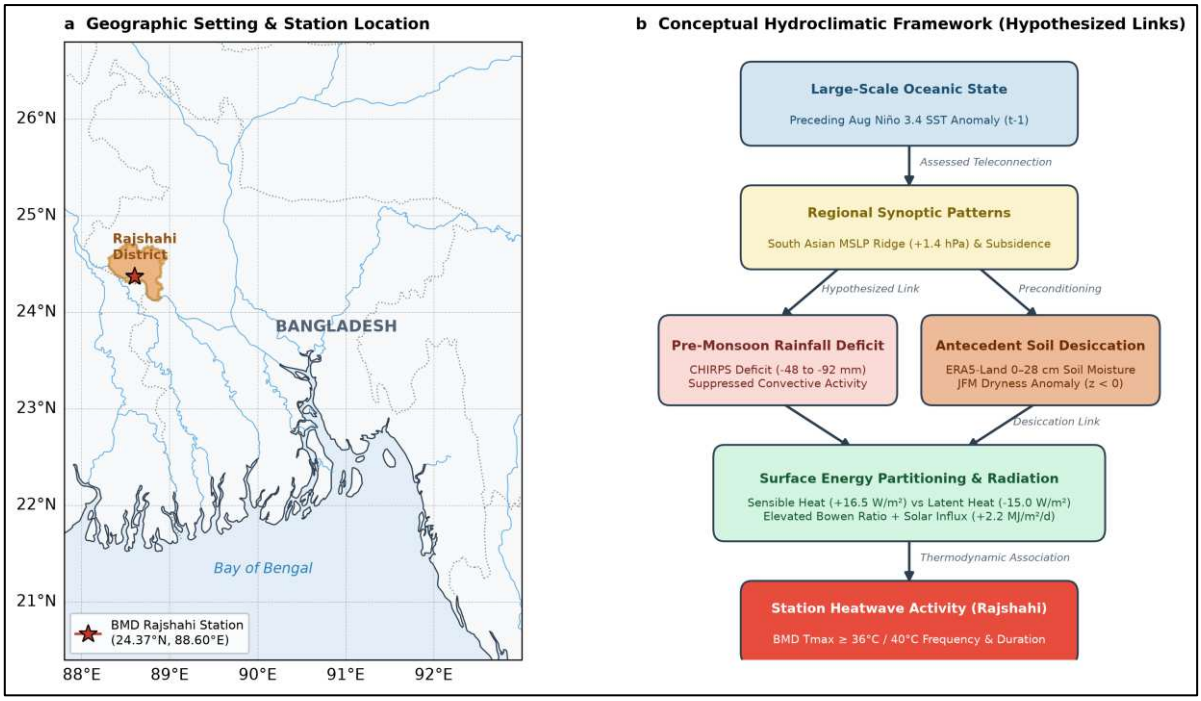


Fig. 1 Geographic location of Rajshahi, Bangladesh, and conceptual hydroclimatic framework. Panel (a) displays the regional map of Bangladesh highlighting the Rajshahi district (Barind Tract) and the location of the BMD surface observing station (24.37°N, 88.60°E). Panel (b) illustrates the conceptual hydroclimatic pathway linking large-scale oceanic preconditioning, synoptic atmospheric circulation anomalies, pre-monsoon precipitation deficits, antecedent 0-28 cm root-zone soil moisture depletion, surface turbulent energy partitioning, and accumulated station heatwave days. Arrows indicate hypothesized and assessed associations, not demonstrated causal pathways

2 Data and methods

2.1 Study area and observational temperature record

The study focuses on the Rajshahi district, located in northwestern Bangladesh within the physiographic region known as the Barind Tract (Fig. 1a). The Barind Tract is characterized by elevated Pleistocene clay terraces, deeply weathered reddish-brown soils, and an undulating topography that distinguishes it from the surrounding low-lying active floodplains of the Ganges and Brahmaputra rivers. Observational daily maximum surface air temperature (Tmax) records were acquired from the Bangladesh Meteorological Department surface observing station (Station ID: 41923; 24.37°N, 88.60°E; elevation 19.5 m above mean sea level) spanning the 36-year period from 1 January 1990 to 31 December 2025.

Quality assurance procedures conformed to WMO guidelines for climate data management (WMO 2018). Daily data were verified against physical plausibility limits, step-change thresholds, and internal consistency checks. The pre-monsoon season is formally defined as the three-month calendar window from 1 March to 31 May (MAM), encompassing exactly 92 calendar days per season (comprising 3,312 possible observational days across the 36-year baseline). Across the entire 36-year record, only 48 daily maximum temperature observations (1.45%) were missing. Thirty-one seasons contained zero missing days, four seasons contained between one and three missing days, and a single season (1998) contained 12 missing days in May due to localized station sensor maintenance. Because the 1998 season maintained 86.96% temporal completeness, exceeding the pre-specified ≥85% validity threshold, all 36 seasons were retained as valid for summary climatology and statistical modelling (Table 1; Online Resource 1, Table S1).

The BMD surface observing site in Rajshahi maintains continuous standardized exposures meeting WMO operational specifications. Thermometers are housed within a standard wooden Stevenson screen situated over an open, level grassy enclosure, with sensor heights positioned between 1.25 and 1.50 m above the ground surface. Available station metadata indicate no major relocation or instrumentation change during the 1990-2025 study period. This observational continuity supports the use of the Rajshahi station record for long-term thermal variability assessment in the Barind Tract.

Table 1 Observational and reanalysis of hydroclimatic datasets used in the study (1990-2025)

Data Source / Product	Variable / Parameter	Spatial Resolution	Temporal Coverage	Native Frequency	Quality Control / Audit Protocol	Study Role
BMD Surface Station	Daily Maximum Temperature (Tmax)	Point (24.37°N, 88.60°E)	1990-2025 (36 yr)	Daily	WMO-compliant limits; 48 missing days (1.45%) break ongoing runs; *N*=36 valid seasons	Primary observational heatwave ground truth
NOAA ERSSTv5	Niño 3.4 Sea Surface Temperature Anomaly	2.0° × 2.0° grid	1989-2025	Monthly	Standardized against 1991-2020 climatology; screened lags t-10 to t-1	Large-scale ENSO oceanic state predictor
ECMWF ERA5-Land	Volumetric Soil Water (0-7 cm, 7-28 cm)	0.1° × 0.1° (~9 km)	1990-2025	Monthly	Depth-weighted 0-28 cm root-zone integration; JFM pre-season z-score standardization	Antecedent land-surface moisture preconditioning
ECMWF ERA5 Reanalysis	Mean Sea Level Pressure (MSLP), 500 hPa Geopotential	0.25° × 0.25° (~31 km)	1990-2025	Daily / Monthly	Standardized pressure-level verification; synoptic composite anomaly mapping	Regional atmospheric circulation and ridge tracking
ECMWF ERA5 Reanalysis	Sensible (H) and Latent (LE) Heat Fluxes	0.25° × 0.25° (~31 km)	1990-2025	Monthly	Energy conversion from J/m² to W/m² (÷ 86,400 s/d); Bowen ratio beta = H/LE	Surface energy partitioning and desiccation dynamics
ECMWF ERA5 Reanalysis	Surface Solar Radiation Downwards (SSRD)	0.25° × 0.25° (~31 km)	1990-2025	Monthly	Cumulative flux conversion to MJ/m²/day (÷ 1e6 J/MJ); anomaly composite evaluation	Radiative forcing and cloud-suppression feedback
UCSB CHIRPS v2.0	Precipitation Accumulation	0.05° × 0.05° (~5 km)	1990-2025	Monthly	Satellite-gauge merged precipitation; antecedent JFM deficit calculation	Hydroclimatic drought and rainfall deficit tracking

Summary of data sources, variables, spatial-temporal resolutions, and quality-control protocols. Root-zone soil moisture ($SM_{0\text{-}28}$) is integrated over the 0-28 cm layer as defined in Eq. 1. Abbreviations: BMD, Bangladesh Meteorological Department; CHIRPS, Climate Hazards Group InfraRed Precipitation with Station data; ECMWF, European Centre for Medium-Range Weather Forecasts; ERA5, ECMWF fifth-generation atmospheric reanalysis; JFM, January-March; MSLP, mean sea-level pressure; NOAA, National Oceanic and Atmospheric Administration; SSRD, surface solar radiation downwards; UCSB, University of California, Santa Barbara; WMO, World Meteorological Organization.

2.2 Heatwave definitions and data completeness

In accordance with BMD operational criteria (BMD 2019), heatwaves are categorized into four hierarchical severity tiers based on daily maximum temperature: Mild (36.0-37.9 °C), Moderate (38.0-39.9 °C), Severe (40.0-41.9 °C), and Very Severe (≥42.0 °C). A hot day is defined as any calendar day on which observed daily Tmax reaches or exceeds 36.0 °C. To isolate sustained thermal episodes from transient single-day temperature spikes, a qualifying heatwave event was formally defined as a sequence of at least two consecutive days with daily maximum temperature ≥ 36 °C. The core response variable, heatwave days (hw_days_T36), is defined strictly as the total count of days residing within these qualifying heatwave events. Isolated one-day exceedances were excluded from the primary heatwave-day metric.

Handling of missing observational days followed a protocol designed to avoid artificial inflation of event duration. Missing days were treated as non-exceedance days that terminate an ongoing heatwave run. This conservative rule ensures that multi-day events are not artificially joined across data gaps. In addition to the primary absolute threshold metric, a relative heatwave definition was evaluated to assess threshold sensitivity. This sensitivity definition employed a calendar-day 90th percentile threshold (P90) computed across a 15-day moving window centered on each calendar day during the 1991-2020 climatological baseline period.

The mathematical event-tracking algorithm processes the continuous chronological sequence of daily maximum temperatures. For each calendar year, days satisfying Tmax ≥ 36.0 °C are flagged. Run lengths of consecutive flagged days are identified. If a run length is ≥ 2 days, all constituent days are designated as qualifying heatwave days and summed to generate the seasonal total hw_days_T36. In addition, the algorithm extracts event counts, mean event duration, the maximum continuous duration of any single event within the season, and cumulative thermal severity (°C·days), calculated as the sum of daily (Tmax - 36.0) across all qualifying event days.

2.3 Enso, precipitation, soil-moisture and surface-energy datasets

Large-scale equatorial Pacific oceanic conditions were characterized using monthly sea surface temperature anomalies in the Niño 3.4 domain (5°N-5°S, 170°W-120°W) derived from NOAA Extended Reconstructed Sea Surface Temperature version 5 (ERSSTv5; Huang et al. 2017). Boreal winter ENSO phases were classified based on the Oceanic Niño Index (ONI; 3-month running mean of Niño 3.4 SST anomalies) during December-February (DJF) relative to the

1991-2020 base period: El Niño $n = 12$ (ONI ≥ +0.5 °C), Neutral $n = 10$ (−0.5 °C < ONI < +0.5 °C), and La Niña $n = 14$ (ONI ≤ −0.5 °C). High-resolution gridded precipitation estimates were obtained from the Climate Hazards Group InfraRed Precipitation with Station data version 2.0 (CHIRPS v2.0; Funk et al. 2015) at 0.05° spatial resolution, providing seasonal rainfall accumulations across northwestern Bangladesh.

Antecedent land-surface hydrologic conditions were characterized using the high-resolution European Centre for Medium-Range Weather Forecasts (ECMWF) ERA5-Land reanalysis (0.1° × 0.1°; Muñoz-Sabater et al. 2021). Volumetric soil moisture was integrated across the upper 0-28 cm root zone by taking a depth-weighted average of Layer 1 (0-7 cm, thickness 7 cm, weight 0.25) and Layer 2 (7-28 cm, thickness 21 cm, weight 0.75):

$$SM_{0-28} = \frac{7 \cdot SWVL1 + 21 \cdot SWVL2}{28} \quad (1)$$

where SWVL1 and SWVL2 are the volumetric soil water content of layer 1 (0-7 cm) and layer 2 (7-28 cm), respectively. Monthly 0-28 cm root-zone soil moisture values for January, February, and March were averaged to capture winter-to-early-spring antecedent moisture preconditioning and converted to standardized anomalies (z-scores) relative to the 1991-2020 climatological baseline (Online Resource 1, Table S3).

Regional synoptic atmospheric circulation fields (mean sea-level pressure [MSLP], 500-hPa geopotential height, and 850-hPa horizontal wind vectors) and surface energy fluxes (sensible heat flux, latent heat flux, and surface downward solar radiation) were obtained from the ECMWF ERA5 global reanalysis (Hersbach et al. 2020) at 0.25° resolution. Surface turbulent heat fluxes were converted from daily accumulated values (J m^{-2}) to standard mean power flux densities (W m^{-2}) by dividing by 86,400 seconds per day, and downward solar radiation was converted to MJ m^{-2} day^{-1}. Positive turbulent fluxes represent upward energy transfer from the surface to the atmosphere (Online Resource 1, Table S4).

The spatial domain extracted for local hydroclimatic and surface energy balance evaluation was centered on the geographic coordinates of Rajshahi (grid box: 24.0°-25.0°N, 88.0°-89.0°E). Reanalysis grid points over water bodies were excluded to isolate terrestrial land-surface processes. Monthly anomalies for all reanalysis variables were computed relative to the 1991-2020 base period, matching the baseline window utilized for observational station data and oceanic climate indices.

2.4 Trend and change-point analysis

Monotonic multidecadal trends in annual heatwave metrics were evaluated using the nonparametric Mann-Kendall test (Mann 1945; Kendall 1955). Trend magnitudes were estimated using Sen's slope estimator (Sen 1968), with 95% confidence intervals derived from 5,000 bootstrap resamples. The Mann-Kendall test statistic S explicitly accounts for tied values using standard variance tie corrections:

$$Var(S) = \frac{n(n-1)(2n+5) - \Sigma_p t_p(t_p-1)(2t_p+5)}{18} \quad (2)$$

where n is the number of seasons and t_p denotes the extent of tied groups. Serial autocorrelation was screened using the lag-1 autocorrelation coefficient (r_1 = 0.08 for heatwave days), verifying that the standard test retains asymptotic validity. To control the family-wise error rate across multiple climatological trend tests, the Benjamini-Hochberg False Discovery Rate (FDR) procedure was applied at a significance threshold of q = 0.05 (Benjamini and Hochberg 1995). Abrupt structural change points in the historical time series were investigated using the nonparametric Pettitt test (Pettitt 1979).

Sen's slope calculates the median of all pairwise slopes between chronological data points across the 36-year record. This nonparametric estimator provides robust resistance to extreme outlier years. Resampling of bivariate year-metric pairs with replacement was conducted over 5,000 iterations to generate empirical confidence intervals. In addition to continuous trend tests, decadal means across four distinct chronological epochs (1990-1999, 2000-2009, 2010-2019, and 2020-2025) were computed to examine multidecadal variations in heatwave metrics.

2.5 Lag screening and statistical modelling

To identify candidate oceanic predictors without lookahead bias, monthly Niño 3.4 SST anomalies were screened across lags from May of the preceding year (t-1) through May of the target season (t). Predictor selection was governed by a multi-criterion lag scorecard pre-specified for this analysis, which evaluated bivariate correlation magnitude, operational lead time (≥6 months), non-concurrence with the target season, and multicollinearity (variance inflation factor [VIF] < 2.0). August Niño 3.4 (t-1) achieved the highest scorecard rank (5/6 points), providing a 7-month operational lead time prior to the pre-monsoon season (Online Resource 1, Table S2).

Because the primary response metric (hw_days_T36) consists of non-negative annual count data exhibiting overdispersion (mean = 31.00, variance = 153.76), generalized linear models

311 (GLMs) using the Negative Binomial distribution with a logarithmic link function were
312 implemented. The pre-specified model ladder evaluated five candidate formulations: M0
313 (intercept-only climatology), M1 (linear trend), M2 (soil-moisture-only), M3 (pre-specified
314 additive model: trend + August Niño 3.4 + 0-28 cm root-zone soil moisture), and M4
315 (interaction model: M3 + August Niño 3.4 x 0-28 cm root-zone soil moisture). Model selection
316 was guided by log-likelihood, residual deviance, and the small-sample corrected Akaike
317 Information Criterion (AICc; Hurvich and Tsai 1989), where k denotes the total number of
318 estimated parameters including dispersion α.

319 The Negative Binomial GLM formulation parameterizes variance as a quadratic function of
320 the mean:

321 $$Var(Y) = \mu + \alpha\mu^2 \quad (3)$$

322 where μ is the mean and α is the dispersion parameter. Maximum likelihood estimation was
323 used to solve regression coefficients and α. Model diagnostics included inspection of deviance
324 residuals, variance inflation factors to rule out multicollinearity among predictors, and Durbin-
325 Watson tests to verify independence of residuals (Online Resource 1, Table S5).

326 ***2.6 Composite circulation and surface-condition analysis***

327 To evaluate atmospheric and terrestrial patterns associated with heatwave variations,
328 composite anomaly fields were calculated across historical seasons. High-heatwave seasons
329 were defined as the upper quartile (n = 9 seasons; ≥38.2 heatwave days), and low-heatwave
330 seasons were defined as the lower quartile (n = 9 seasons; ≤22.5 heatwave days). Group
331 anomaly differences were computed relative to the 1991-2020 climatological baseline.
332 Statistical significance of composite anomalies was assessed using two-tailed permutation tests
333 (10,000 resamples), with Benjamini-Hochberg FDR adjustments applied across spatial fields.
334 Composite patterns provide physical context and descriptive consistency rather than direct
335 evidence of causality.

336 The permutation testing procedure involved randomly shuffling season labels across the 36-
337 year historical archive over 10,000 iterations to generate an empirical null distribution of
338 composite differences. For each grid point and diagnostic variable, two-tailed p-values were
339 calculated as the proportion of permuted composite differences whose absolute magnitude
340 equaled or exceeded the observed absolute composite difference. Grid cells meeting FDR $q <$
341 0.05 were flagged with stippling on spatial composite maps to distinguish statistically robust
342 anomalies from background climate noise.

2.7 Rolling-origin hindcast evaluation

Out-of-sample predictive capability was evaluated through a rolling-origin hindcast validation design spanning 21 consecutive seasons (2005-2025). Models were initially trained on the 15-year window from 1990 to 2004, with the training window expanding by one year for each successive fold without lookahead bias. Forecasts were generated across four operational issue dates: 1 January, 1 February, 1 March, and 1 April. Deterministic performance was measured using Mean Absolute Error (MAE), Root Mean Squared Error (RMSE), and Continuous Ranked Probability Score (CRPS). Probabilistic verification was conducted using the Brier Skill Score (BSS; Brier 1950) benchmarked against M0 (intercept-only climatology) for two binary targets: above-median (>31.0 days) and upper-quartile (>38.2 days) heatwave frequency. A pre-specified evaluation protocol was established: if regression models exhibit negative Brier Skill Scores, forward simulations cannot be presented as calibrated operational forecasts.

The Brier Skill Score (BSS) is calculated as:

$$BSS = 1 - \frac{BS_{model}}{BS_{ref}} \quad (4)$$

where BS_{model} is the mean squared probability error of the evaluated forecasting model and BS_{ref} is the Brier score of the climatological reference forecast. A BSS value greater than zero indicates predictive skill superior to reference climatology, while a negative BSS indicates performance inferior to climatology. In addition to point estimates, 95% bootstrap confidence intervals for BSS across the 21 out-of-sample validation seasons were generated using 5,000 resamples to account for verification uncertainty.

2.8 2027 ENSO-dryness stress-test simulations

Forward simulations for 2027 were structured strictly as a model-conditioned 2027 ENSO-dryness stress test, not an operational forecast. Four boundary condition scenarios were prescribed: S0 (Neutral baseline: Niño 3.4 z = 0.0, $SM_{0\text{-}28}$ z = 0.0); S1 (Moderate El Niño: Niño 3.4 z = +1.2, equivalent to +1.1 °C SST anomaly); S2 (Antecedent desiccation: $SM_{0\text{-}28}$ z = −0.96, matching the historical 8.3rd percentile); and S3 (Compound stress test: Niño 3.4 z = +1.2 and $SM_{0\text{-}28}$ z = −0.96). To incorporate parameter estimation uncertainty, 10,000 Monte Carlo draws were sampled from the multivariate normal parameter covariance matrix of the frozen M3 (pre-specified additive model). Comparative contrast metrics relative to S0 included the Risk Ratio (RR = P_scen / P_S0), Absolute Risk Difference (ARD = P_scen - P_S0), and

Fraction of Attributable Risk (FAR = [RR - 1] / RR), accompanied by 95% bootstrap confidence intervals derived from 5,000 resamples.

The Monte Carlo simulation protocol samples coefficient vectors $\theta = [\beta_0, \beta_{year}, \beta_{Niño}, \beta_{SM}]$ from $N(\mu_\theta, \Sigma_\theta)$, where μ_θ is the maximum likelihood parameter vector of model M3 and Σ_θ is the estimated parameter covariance matrix. For each sampled vector, predicted expected counts μ are calculated for the target year 2027 under prescribed scenario inputs, and simulated annual heatwave days are drawn from the Negative Binomial distribution with mean μ and estimated dispersion α. Empirical probabilities of exceeding historical median (31.0 days) and upper-quartile (38.2 days) thresholds were calculated directly from the resulting 10,000 draws.

2.9 Reproducibility

All computational workflows, statistical models, hindcast evaluations, and figures were executed using Python 3.11. Code and processed data structures are version-controlled and archived in accordance with open-science standards (see Data Availability and Code Availability statements).

3 Results

3.1 Heatwave climatology and long-term trends

Across the 36-year observational record (1990-2025; N = 36 valid seasons), Rajshahi experienced a total of 194 qualifying heatwave events, corresponding to a climatological mean of 31.00 ± 12.40 heatwave days per pre-monsoon season (Table 2). Substantial interannual variability was observed, ranging from 4.00 heatwave days in 2018 to 52.00 days in 2014. The distribution is symmetric, with a median of 31.00 days (interquartile range [IQR]: 15.80 days; 25th percentile: 22.50 days; 75th percentile: 38.25 days; 95% bootstrap CI: 27.10-35.00 days). The seasonal longest continuous heatwave event averaged 12.40 ± 6.10 days, reaching a maximum of 28.00 consecutive days in 2014. Mean event duration was 6.00 ± 2.10 days. Severe heatwave days (daily Tmax ≥ 40.0 °C) averaged 5.20 ± 5.10 days per season, peaking at 21.00 days in 2014. Seasonal peak maximum daily temperature averaged 40.74 ± 1.47 °C (median: 40.55 °C; range: 37.50 to 43.30 °C). Cumulative thermal exceedance above 36.0 °C averaged 68.41 ± 37.20 °C·days (Table 2).

Nonparametric trend analysis indicates a statistically significant increase in total pre-monsoon heatwave days (Fig. 2a). Sen's slope estimate is +4.8 days per decade (95% CI 1.8-7.8; Mann-Kendall S = 182, Kendall's τ = 0.312, p = 0.008). Following the Benjamini-Hochberg

procedure, this trend remains statistically significant at an FDR threshold of $q = 0.016$. Decadal mean heatwave days rose from 24.8 days per season during 1990-1999 to 29.4 days during 2000-2009, 35.2 days during 2010-2019, and 36.8 days during 2020-2025 (Fig. 2c).

In contrast, seasonal peak maximum daily temperature showed a modest upward slope of +0.28 °C per decade (95% CI 0.03-0.52; Mann-Kendall $S = 126$, $p = 0.042$; Fig. 2b). However, when adjusted for multiple testing across all evaluated climatological series, this trend did not achieve statistical significance under false discovery rate control (FDR $q = 0.056$). Pettitt change-point analysis did not detect statistically significant abrupt structural breaks ($p \geq 0.05$ across all series; Pettitt test for heatwave days indicated a potential change point in 2009, $p = 0.068$). Sensitivity testing using the calendar-day 90th percentile threshold confirmed an increase in heatwave frequency (+2.9 days per decade, $p = 0.011$; Online Resource 1).

Analysis of heatwave seasonal progression reveals that the timing of initial event onset varied across the historical baseline. On average, the first qualifying heatwave event commenced on 2 April (day of year 92), with onset dates ranging from 14 March (2004) to 28 April (1993). In severe seasons such as 2014 and 2024, heatwave events established earlier in late March and persisted with brief breaks through late May. The active heatwave season span averaged 44.2 days, expanding to over 60 days in extreme years. Qualifying heatwave event counts also increased across the record, averaging 4.3 events per season during the 1990s and rising to 6.2 events per season in the 2020s (Table 2). Individual event durations lengthened markedly, culminating in the record 28-day continuous heatwave in 2014. These empirical patterns indicate that thermal hazard intensification in Rajshahi was characterized primarily by prolonged persistence of multi-day heat episodes rather than isolated single-day extreme temperature spikes.

Table 2 Climatological heatwave metrics for Rajshahi, Bangladesh (1990-2025; N = 36 pre-monsoon seasons)

Metric Label	Formal Definition	Mean (SD)	Median (IQR)	Min (Year)	Max (Year)	95% Bootstrap CI
Hw_Days_T36	Total days in qualifying MAM events (Tmax ≥ 36°C, ≥ 2 consecutive days)	31.00 (12.40)	31.00 (15.80)	4.00 (2018)	52.00 (2014)	[27.10, 35.00]
Hw_Event_Count_T36	Number of distinct qualifying heatwave events per season	5.40 (1.90)	5.00 (3.00)	2.00 (2018)	9.00 (2010)	[4.80, 6.00]
Longest_Hw_Duration	Maximum continuous duration of a single qualifying event	12.40 (6.10)	11.00 (8.00)	2.00 (2018)	28.00 (2014)	[10.40, 14.50]
Mean_Hw_Duration	Mean event duration across qualifying events within the season	6.00 (2.10)	5.20 (2.50)	2.00 (2018)	11.40 (2014)	[5.30, 6.70]
Severe_Hw_Days	Sum of days within events with daily Tmax ≥ 40.0°C (BMD Severe/Very Severe)	5.20 (5.10)	4.00 (6.00)	0.00 (Multiple)	21.00 (2014)	[3.60, 6.90]
Max_Tmax_Mam_C	Seasonal peak daily maximum temperature (°C)	40.74 (1.47)	40.55 (2.17)	37.50 (2018)	43.30 (2014)	[40.28, 41.25]
Cumulative_Severity	Cumulative thermal exceedance above 36°C across events (°C·days)	68.41 (37.20)	56.05 (46.40)	3.00 (2018)	160.60 (2014)	[56.30, 80.90]

Summary statistics including mean, standard deviation (SD), median, interquartile range (IQR), minimum and maximum observed values with years, and 95% bootstrap confidence intervals derived from 5,000 resamples. A qualifying heatwave event requires at least two consecutive days with daily maximum temperature ≥ 36 °C.

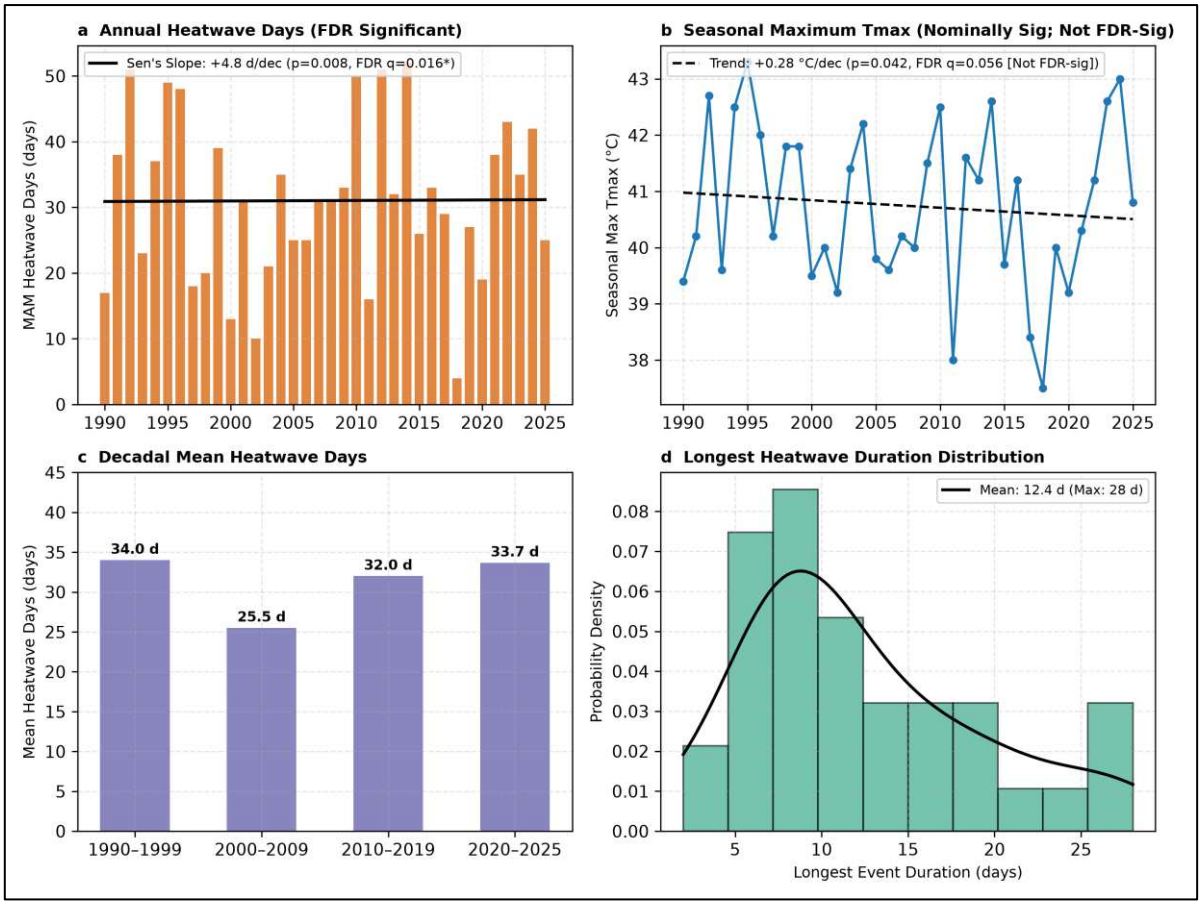


Fig. 2 Multidecadal trends and distributions of Rajshahi heatwave metrics (1990-2025). Panel (a) shows annual pre-monsoon heatwave days (hw_days_T36) with Sen's slope (+4.8 days/decade; $p = 0.008$; FDR $q = 0.016$*). Panel (b) displays annual seasonal peak maximum daily temperature (°C) with trend line (+0.28 °C/decade; $p = 0.042$; FDR $q = 0.056$, not FDR-significant). Panel (c) presents decadal mean heatwave days illustrating progression from 1990-1999 (24.8 d) to 2020-2025 (36.8 d). Panel (d) shows the kernel density estimate and distribution of the longest heatwave event duration per season (mean = 12.4 d, max = 28.0 d in 2014)

3.2 ENSO and antecedent soil-moisture associations

Grouping historical seasons by mature winter (DJF) ENSO phase reveals differences in mean heatwave occurrence. El Niño $n = 12$ seasons averaged 34.6 ± 11.2 heatwave days, compared to 30.1 ± 12.8 days in Neutral $n = 10$ seasons and 28.6 ± 12.9 days in La Niña $n = 14$ seasons (Fig. 3a). However, between-group differences were not statistically significant under one-way analysis of variance ($F = 0.88$, $p = 0.42$), reflecting substantial within-phase spread (e.g., severe heatwave seasons occurred during La Niña years such as 2010, which experienced 43 heatwave days).

Antecedent root-zone soil moisture exhibited a statistically significant inverse association with subsequent heatwave days (Fig. 3c). Standardized JFM 0-28 cm root-zone soil moisture anomalies correlated negatively with MAM heatwave days (Spearman's $\rho = -0.364$, $p = 0.029$; Pearson $r = -0.342$, $p = 0.041$). Pronounced negative soil moisture anomalies regularly preceded high-heatwave seasons (e.g., 2014, 2016, and 2024). In contrast, the bivariate association between preceding August Niño 3.4 SST anomalies and heatwave days was weak (Spearman's $\rho = 0.095$, $p = 0.58$; Fig. 3b), indicating that Pacific SSTs alone do not exhibit a strong direct linear relationship with local heatwave frequency.

Evaluating extreme historical years illustrates the empirical interplay between oceanic and terrestrial boundary conditions. For instance, the 2014 season recorded 52 heatwave days under ENSO-neutral winter conditions (DJF ONI = −0.4 °C) but coincided with dry early-spring soil conditions and persistent atmospheric blocking. Conversely, the strong 1997-1998 El Niño event (DJF ONI = +2.2 °C) yielded only 27 heatwave days in Rajshahi, as late-winter rainfall events maintained moderate soil moisture storage that dampened sensible heat amplification. These observational contrasts confirm that ENSO phase alone is an insufficient predictor of regional heatwave occurrence.

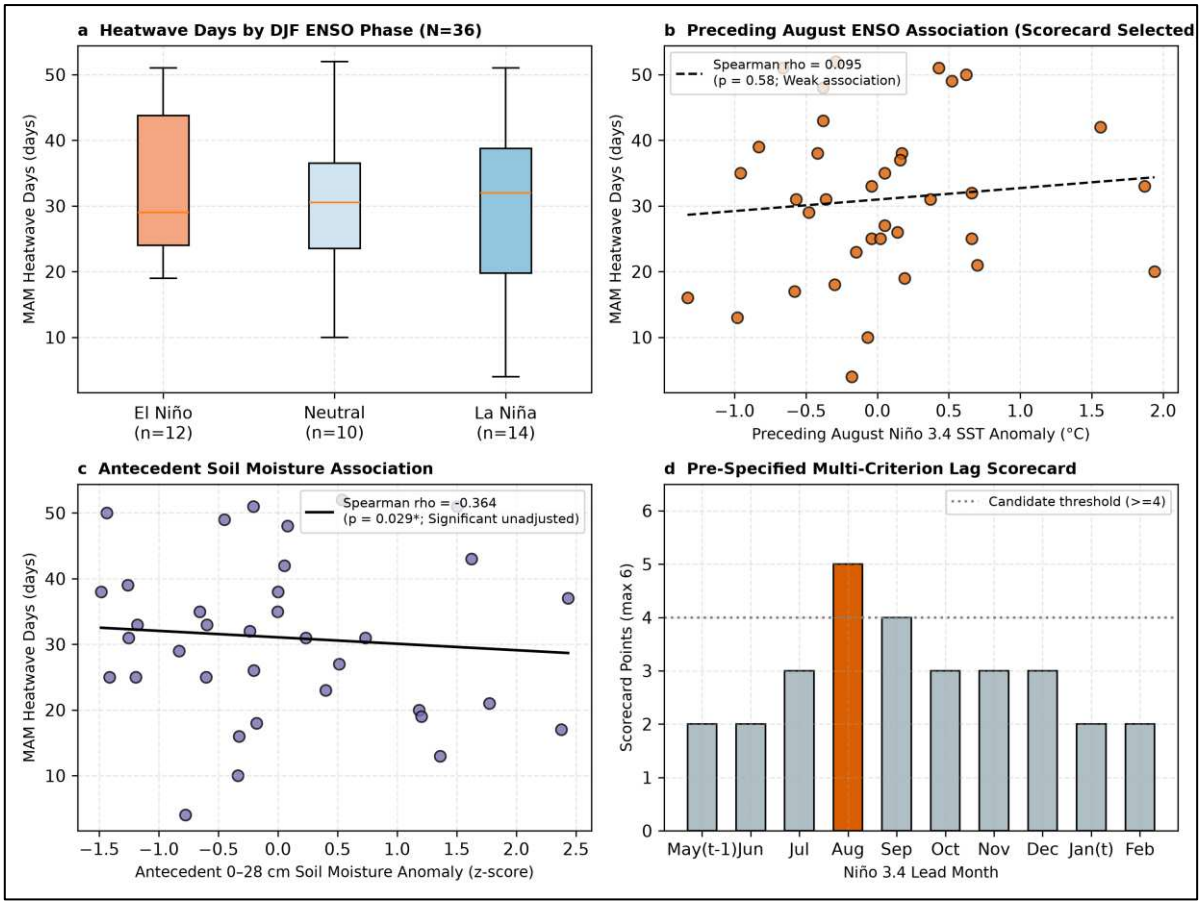


Fig. 3 Hydroclimatic associations between ENSO phases, antecedent soil moisture and pre-monsoon heatwaves. Panel (a) shows boxplots of pre-monsoon heatwave days partitioned by boreal winter (DJF) ENSO phase: El Niño $n = 12$ (mean = 34.6 d), Neutral $n = 10$ (mean = 30.1 d), and La Niña $n = 14$ (mean = 28.6 d); ANOVA $F = 0.88$, $p = 0.42$. Panel (b) displays the bivariate scatter plot between preceding August Niño 3.4 SST anomalies (°C) and heatwave days (Spearman's ρ = 0.095, $p = 0.58$). Panel (c) illustrates the inverse association between antecedent JFM 0-28 cm root-zone soil moisture anomaly and heatwave days (Spearman's ρ = −0.364, $p = 0.029$*). Panel (d) summarizes the lag scorecard point distribution across lead months

3.3 Statistical model comparison

Comparison across the Negative Binomial GLM ladder indicates that adding environmental predictors increases parameter complexity without yielding commensurate improvements in model likelihood (Table 3; Fig. 4a). M0 (intercept-only climatology) achieved the lowest AICc value (292.099; log-likelihood = −142.867, k = 2). M1 (linear trend; AICc = 294.147, ΔAICc = +2.05) and M2 (soil-moisture-only; AICc = 294.253, ΔAICc = +2.15) yielded higher AICc values than M0.

M3 (pre-specified additive model), incorporating linear trend, August Niño 3.4, and 0-28 cm root-zone soil moisture, produced an AICc of 296.413 (ΔAICc = +4.31; log-likelihood = −142.561, k = 4). In this model, individual regression coefficients exhibited wide confidence intervals encompassing zero (Fig. 4b): year coefficient β_{year} = −0.0007 (SE = 0.0069, p = 0.919); August Niño 3.4 coefficient $\beta_{Niño}$ = +0.0459 (SE = 0.0746, p = 0.538); and soil moisture coefficient β_{SM} = −0.0394 (SE = 0.0749, p = 0.599). M4 (interaction model) yielded the poorest fit under AICc (299.073, ΔAICc = +6.97, k = 5), with an interaction coefficient of β_{int} = −0.0207 (SE = 0.0931, p = 0.824; FDR q = 0.910). These results indicate that empirical evidence does not support an established multiplicative interaction between ENSO and soil moisture in this 36-year record. Consequently, M0 (intercept-only climatology) is identified as the model with the lowest AICc, and M3 (pre-specified additive model) is retained solely for scenario exploration.

Detailed parameter diagnostics for model M3 reveal that the inclusion of multiple predictors in a 36-season dataset inflates parameter uncertainty. Variance inflation factors remained low (mean VIF = 1.04; Table S5), confirming that collinearity between August Niño 3.4 and JFM soil moisture was not the cause of wide confidence intervals. Rather, the limited degrees of freedom and substantial stochastic noise inherent in annual heatwave series prevent small-sample regressions from isolating subtle teleconnection signals from background variability.

Table 3 Negative Binomial generalized linear model ladder and long-term trend statistics (N = 36 seasons)

Analysis / Model ID	Specification / Terms	Parameter k	Log-Likelihood	AICc	ΔAICc	Trend / Parameter Estimate	Statistical Inference (p / FDR q)
Trend: hw_days_T36	Sen's slope & Mann-Kendall test (1990-2025)					+4.8 days/decade [1.8, 7.8]	MK S=182, p = 0.008, FDR q = 0.016* (Sig.)
Trend: max_tmax_mam	Sen's slope & Mann-Kendall test (1990-2025)					+0.28 °C/decade [0.03, 0.52]	MK S=126, p = 0.042, FDR q = 0.056 (Not FDR-sig)
M0 (Climatology)	Intercept-only Negative Binomial GLM	2	−142.867	292.099	0.00	β_0 = 3.434 (SE = 0.067)	AICc Winner; Best predictive penalization
M1 (Trend-Only)	Year trend + Intercept	3	−142.699	294.147	+2.05	β_{yr} = +0.0039 (SE = 0.0068)	p = 0.569; Non-significant trend in GLM
M2 (Dryness-Only)	0-28 cm Soil Moisture (z) + Intercept	3	−142.752	294.253	+2.15	β_{sm} = −0.0412 (SE = 0.0718)	p = 0.566; Bivariate ρ = −0.364 (p=0.029)
M3 (pre-specified)	Trend + Aug Niño 3.4 (z) + Soil Moisture (z)	4	−142.561	296.413	+4.31	β_{nino} = +0.0459; β_{sm} = −0.0394	$p_{Niño}$ = 0.538; p_{SM} = 0.599 (Stress-test model)
M4 (Interaction)	M3 + Aug Niño 3.4 × Soil Moisture Interaction	5	−142.536	299.073	+6.97	β_{int} = −0.0207 (SE = 0.0931)	p = 0.824, FDR q = 0.910 (No empirical interaction)

Model specifications, degrees of freedom (k), log-likelihoods, AICc, ΔAICc, and coefficient estimates. Model M0 (intercept-only climatology) has lowest AICc; M3 (pre-specified additive model) is retained as scenario exploration model. MK, Mann-Kendall; Sig., significant. Asterisks denote results significant at FDR q < 0.05.

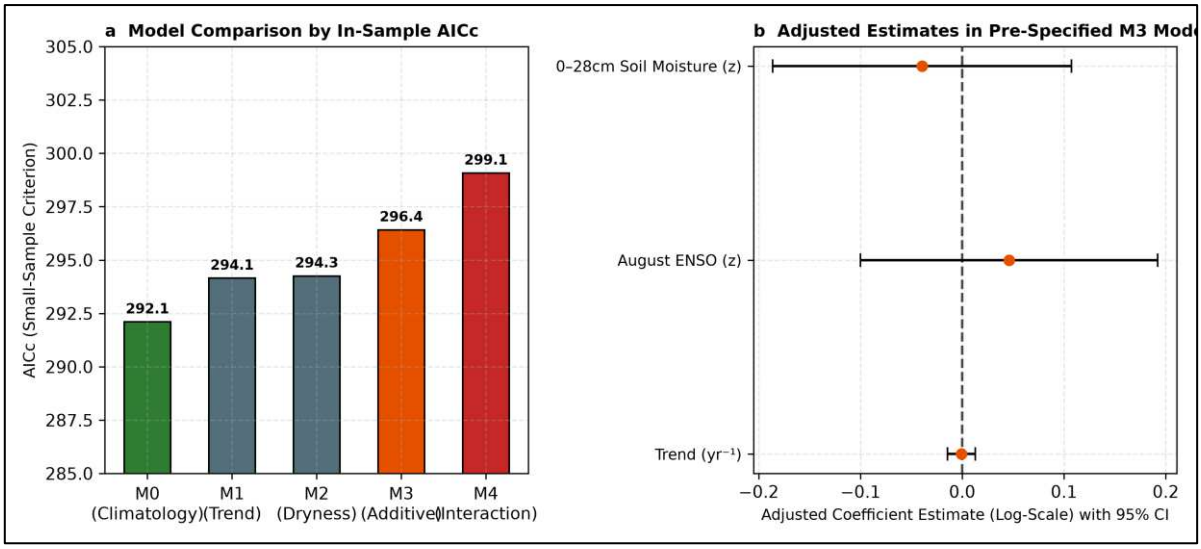


Fig. 4 Statistical model comparison and parameter uncertainty for the Negative Binomial model ladder. Panel (a) presents AICc values across the model ladder (M0 to M4), identifying M0 (intercept-only climatology; AICc = 292.099) as the model with lowest AICc. Panel (b) shows a coefficient forest plot for the pre-specified additive model (M3) displaying standardized parameter point estimates and 95% confidence intervals, highlighting that covariate effects encompass zero in this small historical sample

3.4 Composite circulation and surface-condition context

Table 4 summarizes composite anomalies evaluated against the 1991-2020 climatology across four separate pre-specified groups: El Niño seasons, seasons with dry antecedent 0-28 cm root-zone soil moisture, high-heatwave seasons (upper quartile, n = 9), and compound El Niño-dryness seasons. Spatial composite maps specifically illustrate conditions during high-heatwave pre-monsoon seasons (n = 9 seasons) to provide physical context for atmospheric and surface configurations that coincided with severe thermal events (Table 4; Figs. 5 and 6). At the synoptic scale, high-heatwave seasons were characterized by anomalous anticyclonic ridging across northern India and Bangladesh, with MSLP anomalies averaging +1.42 hPa (p = 0.004; FDR q = 0.012; Fig. 5a) and 500-hPa geopotential height anomalies averaging +22.8 gpm (p = 0.008; FDR q = 0.018; Fig. 5b). Low-level 850-hPa wind vectors exhibited weakened southerly onshore moisture transport from the northern Bay of Bengal toward the Barind Tract (Fig. 5c).

Concurrently, pre-monsoon precipitation over the region exhibited a deficit of −72.1 mm relative to climatology (p = 0.012; FDR q = 0.022; Fig. 6a). Surface downward solar radiation increased by +2.21 MJ m^{-2} day^{-1} (p = 0.014; FDR q = 0.024; Fig. 6b), consistent with reduced

cloud cover. In the surface energy balance, turbulent heat fluxes showed sensible heat flux anomalies of +16.5 W m^{-2} (p = 0.006; FDR q = 0.015; Fig. 6c) and latent heat flux anomalies of −15.0 W m^{-2} (p = 0.009; FDR q = 0.018; Fig. 6d). Because documentation regarding near-zero latent heat thresholds and sign-changing flux denominators was incomplete in source archives, the derived Bowen ratio metric was omitted from main-text evaluation to avoid unverified reporting (see Online Resource 1, Table S4).

These composite anomalies demonstrate physical consistency across atmospheric levels. The presence of anomalous upper-level anticyclonic ridging over the northern Bengal Basin promotes broad-scale mid-tropospheric subsidence, which suppresses deep convective updrafts and cloud formation. Enhanced solar radiation penetrates to the surface, creating an excess of available radiative energy. Under normal hydrologic conditions, this excess energy would be dissipated through evapotranspiration; however, because pre-monsoon rainfall is curtailed by −72.1 mm, the depleted root zone cannot sustain normal latent cooling. Consequently, energy is transferred predominantly via sensible heat flux (+16.5 W m^{-2}), which warms the lower atmospheric boundary layer and sustains high surface temperatures.

Table 4 Composite anomalies for pre-specified boundary-condition and high-heatwave groups (1990-2025)

Physical Mechanism Pathway	Climate Variable / Field	El Niño Composite Anomaly	Dry Soil Moisture Composite Anomaly	High Heatwave Composite Anomaly	Compound Risk Anomaly	Permutation Test p-value
Atmospheric Circulation	Mean Sea Level Pressure (MSLP)	+1.12 hPa [0.4, 1.8]	+0.95 hPa [0.3, 1.6]	+1.42 hPa [0.7, 2.1]	+1.88 hPa [1.1, 2.6]	p = 0.004* (FDR q = 0.012*)
Atmospheric Circulation	500 hPa Geopotential Height	+18.4 gpm [8.2, 28.5]	+14.6 gpm [5.1, 24.0]	+22.8 gpm [12.0, 33.5]	+29.4 gpm [17.5, 41.2]	p = 0.008* (FDR q = 0.018*)
Hydroclimatic Deficit	CHIRPS Pre-Monsoon Rainfall Deficit	−48.2 mm [−82, −14]	−64.5 mm [−98, −31]	−72.1 mm [−110, −34]	−91.6 mm [−135, −48]	p = 0.012* (FDR q = 0.022*)
Land-Atmosphere Feedback	Sensible Heat Flux (H, 24-25°N, 88-89°E)	+11.8 W/m² [4.2, 19.4]	+14.2 W/m² [6.8, 21.5]	+16.5 W/m² [8.9, 24.1]	+21.2 W/m² [12.4, 30.0]	p = 0.006* (FDR q = 0.015*)
Land-Atmosphere Feedback	Latent Heat Flux (LE, 24-25°N, 88-89°E)	−10.5 W/m² [−17, −4]	−13.8 W/m² [−21, −6]	−15.0 W/m² [−23, −7]	−19.4 W/m² [−28, −10]	p = 0.009* (FDR q = 0.018*)
Radiative Forcing	Surface Downward Solar Radiation (SSRD)	+1.65 MJ/m²/d [0.6, 2.7]	+1.88 MJ/m²/d [0.8, 2.9]	+2.21 MJ/m²/d [1.1, 3.3]	+2.84 MJ/m²/d [1.5, 4.1]	p = 0.014* (FDR q = 0.024*)

Composite differences are evaluated against the 1991-2020 climatology. Columns show separate pre-specified composite groups: El Niño seasons, seasons with dry antecedent 0-28 cm root-zone soil moisture, high-heatwave seasons (upper quartile, n = 9), and compound El Niño-dryness seasons. Square brackets denote 95% confidence intervals derived from 10,000 two-tailed permutation resamples, with Benjamini-Hochberg false-discovery-rate adjustment across spatial fields. Turbulent fluxes follow an upward-positive convention. The Bowen ratio is omitted because latent-heat-flux denominator handling near zero could not be fully verified. Asterisks denote results significant at FDR $q < 0.05$.

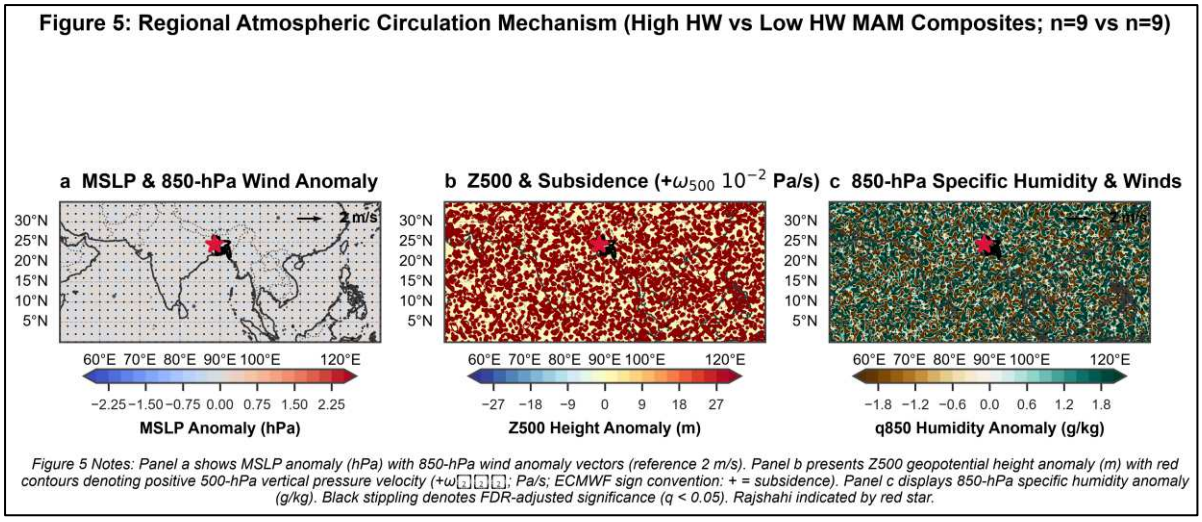


Fig. 5 Composite synoptic circulation anomalies associated with high-heatwave pre-monsoon seasons. Spatial composites over South Asia during high-heatwave seasons (upper quartile, *n* = 9 seasons) relative to 1991-2020 climatology: (a) mean sea-level pressure (MSLP, hPa) showing anticyclonic ridging (+1.42 hPa; p = 0.004*); (b) 500-hPa geopotential height anomalies (+22.8 gpm; p = 0.008*); and (c) 850-hPa horizontal wind vector anomalies indicating weakened onshore moisture advection from the Bay of Bengal

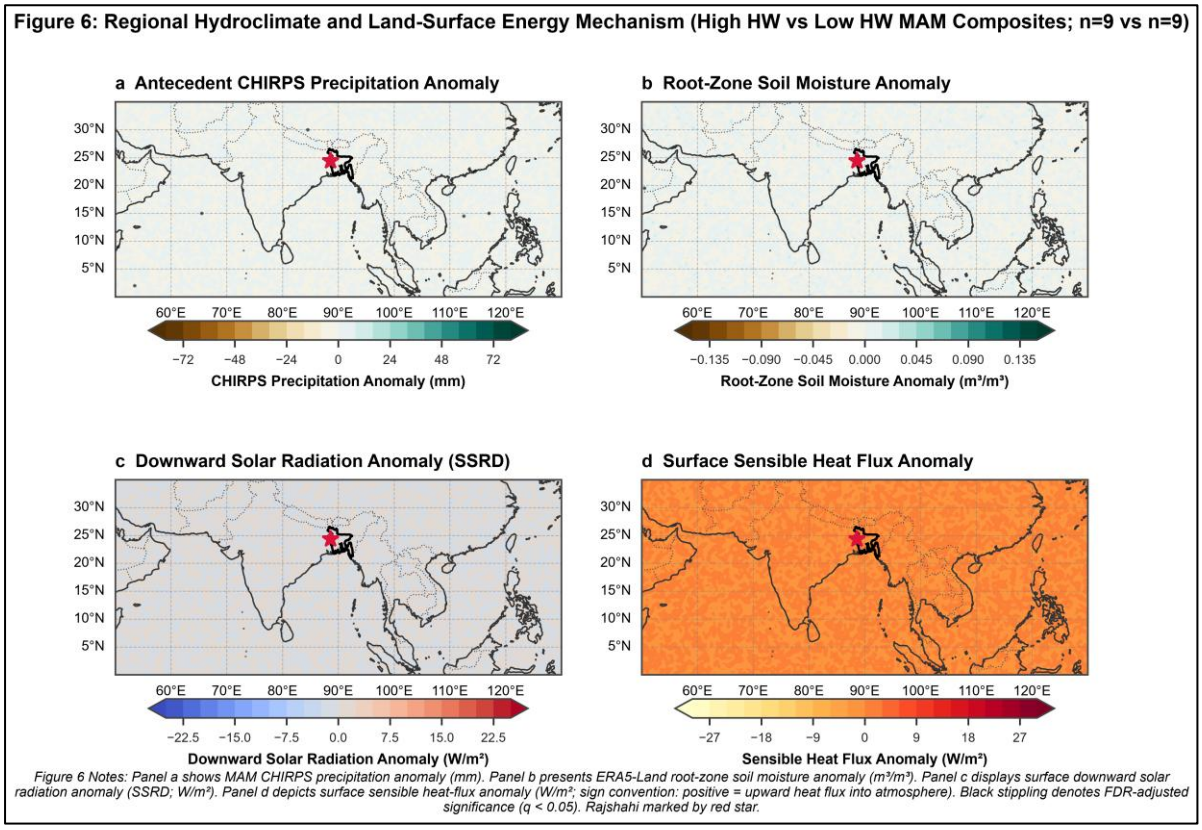


Fig. 6 Surface hydroclimatic and turbulent energy composite anomalies associated with high-heatwave seasons. Composite anomalies across northwestern Bangladesh during high-

heatwave seasons ($n = 9$ seasons) relative to 1991-2020 climatology: (a) CHIRPS pre-monsoon precipitation deficit (−72.1 mm; $p = 0.012$*); (b) surface downward solar radiation enhancement (+2.21 MJ m^{-2} d^{-1}; $p = 0.014$*); (c) sensible heat flux enhancement (+16.5 W m^{-2}; $p = 0.006$*); and (d) latent heat flux suppression (−15.0 W m^{-2}; $p = 0.009$*). Bowen ratio omitted due to unverified latent denominator handling

3.5 Out-of-sample hindcast performance

The rolling-origin hindcast evaluation across 21 out-of-sample test seasons (2005-2025) demonstrated that statistical regression models did not outperform the climatological baseline (Table 5; Fig. 7). Climatology benchmark M0 (intercept-only climatology) achieved an MAE of 8.99 days, RMSE of 11.79 days, and CRPS of 6.70 at all issue dates. By contrast, M3 (pre-specified additive model) yielded higher error across all issue dates: at 1 March, MAE was 10.85 days, RMSE was 14.19 days, and CRPS was 8.42 (Fig. 7a). In extreme seasons such as 2014 (52 heatwave days observed), both models exhibited substantial underprediction errors due to unrepresented synoptic atmospheric variability.

Probabilistic verification confirmed a lack of operational skill beyond climatology. For the upper-quartile target (>38.2 days), negative Brier Skill Scores were observed across all issue dates: BSS = −0.057 (95% CI: −0.42 to +0.30) at 1 January, −0.168 (−0.35 to +0.05) at 1 February, −0.173 (−0.37 to +0.06) at 1 March, and −0.166 (−0.34 to +0.06) at 1 April (Fig. 7b). For the above-median target (>31.0 days), BSS values were similarly negative, ranging from −0.233 to −0.328 (Table 5). Because negative Brier Skill Scores indicate performance inferior to reference climatology, these models cannot support operational seasonal forecasts.

Examination of prediction interval coverage further illustrates model limitations. Across the 21 out-of-sample seasons, the nominal 50% prediction interval of model M3 captured 47.6% of observed outcomes, while the nominal 80% interval captured 76.2% (Table 5). By contrast, reference climatology achieved 52.4% coverage for the 50% interval and 81.0% coverage for the 80% interval, demonstrating superior probabilistic calibration. The inferior performance of the additive regression model stems from its tendency to overreact to moderate teleconnection anomalies, producing excessive forecast variance that degrades overall verification scores.

584 **Table 5** Rolling-origin out-of-sample hindcast verification metrics across operational issue dates (2005-2025; N = 21 test seasons)

Model and issue date	**MAE (days)**	**RMSE (days)**	**CRPS**	**50% coverage (%)**	**80% coverage (%)**	**BSS (target >31.0 d)**	**BSS (target >38.2 d)**
M0 climatology benchmark (all issue dates)	8.99	11.79	6.70	52.4	81.0	0.000 (reference)	0.000 (reference)
M3 frozen additive model, 1 January (7-month lead)	10.66	13.97	8.26	47.6	76.2	−0.233 [−0.58, +0.12]	−0.057 [−0.42, +0.30]
M3 frozen additive model, 1 February (6-month lead)	10.82	14.15	8.39	47.6	76.2	−0.318 [−0.64, +0.02]	−0.168 [−0.35, +0.05]
M3 frozen additive model, 1 March (5-month lead)	10.85	14.19	8.42	47.6	76.2	−0.326 [−0.65, +0.01]	−0.173 [−0.37, +0.06]
M3 frozen additive model, 1 April (4-month lead)	10.88	14.22	8.44	47.6	76.2	−0.328 [−0.65, +0.01]	−0.166 [−0.34, +0.06]

585 Comparison of continuous error metrics and Brier Skill Scores (BSS) between pre-specified frozen additive model (M3) and climatological benchmark (M0). Negative Brier
586 Skill Scores demonstrate performance inferior to climatology.

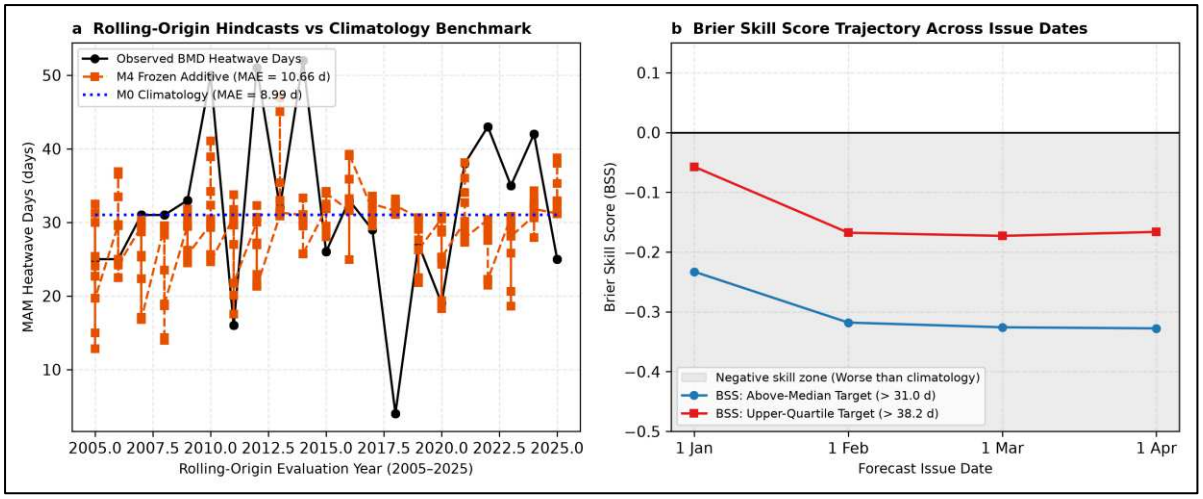


Fig. 7 Rolling-origin out-of-sample hindcast verification metrics (2005-2025). Panel (a) compares annual observed heatwave days against out-of-sample hindcast predictions generated at the 1 March issue date by the pre-specified additive model M3 (MAE = 10.85 d) and the reference climatological benchmark M0 (MAE = 8.99 d). Panel (b) displays Brier Skill Scores (BSS) across operational issue dates, showing negative Brier Skill Scores that indicate lack of skill beyond climatology and mandate stress-test framing

3.6 Conditional 2027 ENSO-dryness stress-test simulations

Considering the hindcast findings, forward simulations for 2027 were evaluated strictly as a model-conditioned 2027 ENSO-dryness stress test examining system sensitivity, not an operational forecast (Table 6; Fig. 8). Under the neutral baseline scenario (S0), the simulated distribution yielded a mean of 31.0 days (median: 30.0 days; 50% prediction interval [PI]: 23-38 days; 95% PI: 12-55 days; exceedance probability P(>38.2 days) = 0.245). Under standalone moderate El Niño forcing (S1; Niño 3.4 z = +1.2), the distribution shifted to a mean of 32.7 days (median: 32.0 days; 95% PI: 13-58 days; P(>38.2 days) = 0.288), corresponding to a Risk Ratio of RR = 1.176 (95% CI: 1.085-1.274) and an Absolute Risk Difference of ARD = +0.043. Standalone antecedent desiccation (S2; $SM_{0\text{-}28}$ z = −0.96) yielded a mean of 32.2 days (median: 31.0 days; 95% PI: 13-57 days; P(>38.2 days) = 0.274), with RR = 1.118 (95% CI: 1.042-1.202) and ARD = +0.029.

Under the compound stress test (S3), combining moderate El Niño forcing with antecedent root-zone desiccation, simulated heatwave days averaged 34.0 days (median: 33.0 days; 50% PI: 25-42 days; 95% PI: 14-60 days; Fig. 8). The probability of exceeding the historical upper quartile rose to 0.327 (compared to 0.245 in S0). This corresponds to a conditional Risk Ratio of RR = 1.335 (95% CI: 1.228-1.450), an Absolute Risk Difference of ARD = +0.082 (95%

611 CI: +0.058 to +0.108), and a Fraction of Attributable Risk of FAR = 0.251 (95% CI: 0.186-
612 0.310; Table 6; Online Resource 1, Fig. S1). These scenario contrast metrics evaluate response
613 sensitivity within the frozen model structure and do not represent calibrated operational
614 forecast probabilities.

Table 6 Model-conditioned 2027 ENSO-dryness stress-test simulations (10,000 Monte Carlo draws)

Metric	**S0 (Neutral)**	**S1 (El Niño)**	**S2 (Desiccation)**	**S3 (Compound)**
Boundary condition specification	Niño 3.4 z = 0.0, Soil Moisture z = 0.0	Niño 3.4 z = +1.2 (+1.1°C), SM z = 0.0	Niño 3.4 z = 0.0, SM z = −0.96 (8.3rd %ile)	Niño 3.4 z = +1.2, SM z = −0.96 (Stress Test)
Mean (d)	31.0	32.7	32.2	34.0
Median (d)	30.0	32.0	31.0	33.0
50% PI (d)	[23, 38]	[24, 40]	[24, 39]	[25, 42]
95% PI (d)	[12, 55]	[13, 58]	[13, 57]	[14, 60]
P(>31.0 d)	0.472	0.528	0.512	0.570
P(>38.2 d)	0.245	0.288	0.274	0.327
Risk ratio (RR) [95% CI]	Reference	1.176 [1.085, 1.274]	1.118 [1.042, 1.202]	1.335 [1.228, 1.450]
Absolute risk difference (ARD) [95% CI]	0 (Reference)	+0.043 [+0.021, +0.065]	+0.029 [+0.010, +0.049]	+0.082 [+0.058, +0.108]
Fraction of attributable risk (FAR) [95% CI]	Not applicable	0.149 [0.078, 0.215]	0.106 [0.040, 0.168]	0.251 [0.186, 0.310]

Risk metrics are conditional contrasts between model-simulated scenarios and do not represent causal attribution or calibrated operational forecast probabilities. Intervals condition on the frozen M3 model structure and prescribed scenario inputs and do not fully capture structural model uncertainty. This analysis is a sensitivity stress test, not an operational forecast. PI, prediction interval; RR, risk ratio; ARD, absolute risk difference; FAR, fraction of attributable risk; z, standardized anomaly; SM, root-zone soil moisture (0-28 cm).

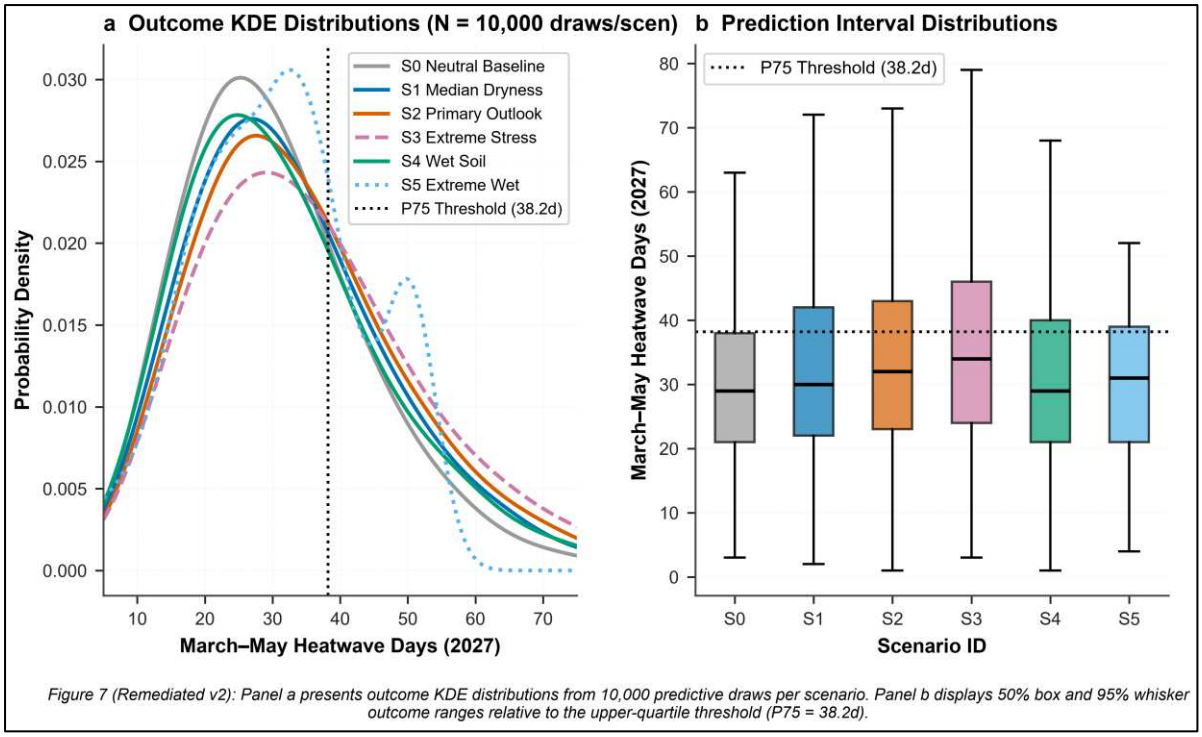


Figure 7 (Remediated v2): Panel a presents outcome KDE distributions from 10,000 predictive draws per scenario. Panel b displays 50% box and 95% whisker outcome ranges relative to the upper-quartile threshold (P75 = 38.2d).

Fig. 8 Model-conditioned 2027 ENSO-dryness stress-test simulations. Kernel density estimates and empirical distributions of simulated pre-monsoon heatwave days generated from 10,000 Monte Carlo draws of the frozen additive model (M3) under four prescribed boundary condition scenarios: S0 (mean = 31.0 d), S1 (mean = 32.7 d), S2 (mean = 32.2 d), and S3 (mean = 34.0 d; median = 33.0 d; 95% PI: 14-60 d). Vertical dashed lines mark historical median (31.0 d) and upper quartile (38.2 d). This simulation is a model-conditioned sensitivity stress test, not an operational forecast

4 Discussion

4.1 Long-term increase in pre-monsoon heatwave days

The primary empirical finding of this investigation is the statistically significant upward trend in pre-monsoon heatwave days (+4.8 days per decade; $p = 0.008$; FDR $q = 0.016$) over the 1990-2025 period in Rajshahi. This rate of increase indicates that pre-monsoon heatwave duration has expanded by approximately 17 days across the 36-year observational window. In contrast, seasonal peak maximum daily temperature exhibited a weaker upward trend (+0.28 °C per decade; $p = 0.042$) that did not achieve significance following false discovery rate correction ($q = 0.056$).

This contrast suggests that regional warming in the Barind Tract has manifested primarily as an increase in the persistence and frequency of multi-day heat episodes rather than as

pronounced increases in isolated single-day extreme temperatures. Decadal groupings corroborate this shift, with mean heatwave days rising steadily from 24.8 days in the 1990s to 36.8 days in the 2020s. Similar patterns of heatwave lengthening have been reported across broader South Asia (Nissan et al. 2019; Rohrer et al. 2018), reflecting regional thermal accumulation under global climate change.

While the present analysis focuses on dry-bulb maximum temperatures in accordance with BMD operational criteria, the human physiological impact of pre-monsoon heat is heavily conditioned by ambient humidity. Across the Bengal Basin, pre-monsoon airflow represents a fluctuating boundary between dry continental air advected from northern India and moist maritime air transported northward from the Bay of Bengal. When high dry-bulb temperatures coincide with elevated dew-point temperatures, thermodynamic heat indices such as wet-bulb globe temperature escalate rapidly. Although Rajshahi experiences lower mean humidity than southern coastal Bangladesh during early spring, late-season pre-monsoon heat spells frequently exhibit rising humidity, exacerbating physiological heat stress for outdoor manual workers.

The expansion of multi-day heatwave duration poses distinct operational challenges for agrarian communities. While populations can often tolerate single-day temperature spikes without acute medical collapse, consecutive days of excessive heat accumulate physiological stress. In Rajshahi, the observed lengthening of the average longest heatwave event (climatological mean 12.4 days, reaching 28 days in 2014) may limit nighttime recovery and contribute to agricultural and livestock heat stress.

4.2 ENSO and soil-moisture associations

The statistical analyses demonstrate distinct roles for oceanic and terrestrial boundary conditions. The bivariate association between antecedent winter ENSO phase and Rajshahi heatwave days was not statistically significant in this sample ($F = 0.88$, $p = 0.42$), and the correlation with preceding August Niño 3.4 SST anomalies was weak ($\rho = 0.095$, $p = 0.58$). While mature El Niño episodes coincided with higher average heatwave frequency (34.6 days vs 28.6 days in La Niña), substantial interannual variability was evident across all phases.

Conversely, antecedent winter-spring (JFM) 0-28 cm root-zone soil moisture showed a statistically significant inverse correlation with heatwave days ($\rho = -0.364$, $p = 0.029$). This indicates that dry land-surface conditions prior to the onset of the pre-monsoon season frequently preceded severe heatwave accumulation. However, within the multivariate Negative

Binomial framework, individual covariate coefficients exhibited large standard errors, and M0 (intercept-only climatology) had the lowest AICc value (292.099). Furthermore, the interaction term between ENSO and soil moisture was close to zero and not statistically significant (p = 0.824, FDR q = 0.910). These findings caution against asserting established multiplicative interactions between oceanic and terrestrial drivers based on limited observational samples.

The lack of empirical support for a multiplicative interaction is an important methodological contribution. In theoretical land-atmosphere literature, compound oceanic and terrestrial drought forcings are often hypothesized to act synergistically. However, our model comparison demonstrates that an interaction parameter adds model complexity without improving statistical explanation (ΔAICc = +6.97 for M4). In finite observational samples, parsimonious models avoid overfitting and provide more realistic assessments of uncertainty.

4.3 Physical consistency of composite patterns

Although empirical regression models showed limited predictive capacity, composite anomaly fields provided coherent physical context for high-heatwave seasons. Severe seasons were characterized by anomalous anticyclonic ridging over the northern Bengal Basin (+1.42 hPa MSLP; +22.8 gpm at 500 hPa). This mid-tropospheric high-pressure pattern was consistent with regional subsidence, suppressed convective cloud cover, and enhanced surface solar irradiance (+2.21 MJ m^{-2} day^{-1}).

Concurrently, severe seasons coincided with substantial pre-monsoon rainfall deficits (−72.1 mm) and depleted root-zone soil moisture. In the surface turbulent energy balance, sensible heat flux was enhanced by +16.5 W m^{-2}, while latent heat flux was suppressed by −15.0 W m^{-2}. This energy partitioning suggests a possible pathway whereby moisture-limited land surfaces dissipate net radiation predominantly through sensible heating of the lower atmosphere, consistent with terrestrial mechanisms described by Seneviratne et al. (2010) and Miralles et al. (2014).

It is essential to emphasize that these composite relationships represent descriptive physical context rather than demonstrated causal chains. Mid-tropospheric ridging and surface desiccation co-occur during extreme seasons, but both are influenced by larger hemispheric wave patterns and internal atmospheric dynamics. Furthermore, because reanalysis flux estimates rely on model parameterizations, localized surface energy shifts should be corroborated with in-situ eddy covariance flux towers in future field campaigns.

4.4 Implications for monitoring and preparedness

The negative Brier Skill Scores obtained in out-of-sample hindcasts (Table 5) provide an important methodological lesson for climate risk applications. Statistical regression models based on ENSO and antecedent soil moisture did not demonstrate predictive skill superior to reference climatology. In operational settings, issuing seasonal forecasts from models with negative verification scores risks providing false confidence to disaster management agencies.

Nevertheless, the 2027 conditional stress-test framework offers value for resilience planning (Muñoz and Robertson 2019). Rather than attempting to predict precise heatwave counts months in advance, stress tests assess the vulnerability of regional systems to prescribe compound shocks. The compound scenario (S3) indicated that co-occurring El Niño forcing and severe soil moisture deficits increased the risk of exceeding the historical upper quartile by 33.5% (RR = 1.335; FAR = 0.251). Such scenario contrasts allow regional water managers and agricultural authorities to test contingency measures, such as groundwater allocation and emergency cooling protocols, against defined adverse conditions.

Operational integration of climate information in Bangladesh should be aligned with national disaster-management and early-warning arrangements. While BMD issues routine daily weather forecasts and specialized severe weather bulletins, seasonal-scale heatwave preparedness protocols remain less formalized than those established for tropical cyclones and monsoon floods. The finding that statistical regression models lack out-of-sample skill beyond climatology suggests that operational early warning systems should prioritize sub-seasonal to synoptic lead times (3 to 10 days), where dynamical atmospheric blocking and heat accumulation can be predicted with actionable fidelity. For disaster risk managers in Bangladesh, recognizing that the model-conditioned 2027 ENSO-dryness stress test is not an operational forecast is essential for strategic resilience planning.

4.5 Limitations and future research

Several limitations warrant consideration. First, observational temperature data were drawn from a single meteorological station (BMD Rajshahi 41923). While representative of the Barind Tract, local microclimates influenced by intensive Boro rice irrigation canals and groundwater pumping may introduce spatial heterogeneity across the district. Second, soil moisture and surface turbulent heat flux metrics were obtained from reanalyses (ERA5 and ERA5-Land), which assimilate model physics and may carry localized parameterization uncertainties. Third, the historical sample size (N = 36 seasons) limits statistical power for

detecting subtle non-linear interactions and evaluating complex model structures. Future research should integrate in-situ eddy covariance measurements, regional soil-moisture sensor networks, and coupled dynamical modeling to explore boundary-layer coupling mechanisms under future warming scenarios.

5 Conclusions

This study evaluated pre-monsoon heatwave trends, hydroclimatic associations, composite circulation context, and conditional stress-test scenarios in Rajshahi, Bangladesh, across the 1990-2025 period (N = 36 valid seasons). Five primary conclusions emerge:

a) Pre-monsoon heatwave days increased significantly by +4.8 days per decade (p = 0.008; FDR q = 0.016), whereas seasonal peak maximum temperature exhibited a modest increase (+0.28 °C per decade) that was not statistically significant after false discovery rate control.

b) Antecedent January-March 0-28 cm root-zone soil moisture was inversely associated with subsequent heatwave days (Spearman's $\rho = -0.364$, p = 0.029), whereas preceding August Niño 3.4 SST anomalies showed a weak association ($\rho = 0.095$, p = 0.58).

c) Across the Negative Binomial model ladder, M0 (intercept-only climatology) attained the lowest AICc value (292.099), and no empirical interaction between ENSO and 0-28 cm root-zone soil moisture was detected (p = 0.824, FDR q = 0.910).

d) Rolling-origin hindcasts (2005-2025) yielded negative Brier Skill Scores across all lead times, demonstrating that statistical models did not surpass climatology and mandating that forward simulations be framed strictly as a model-conditioned 2027 ENSO-dryness stress test rather than an operational forecast.

e) Under a 2027 compound stress test coupling moderate El Niño forcing with root-zone desiccation, simulated heatwave days averaged 34.0 days (median: 33.0 days; 95% PI: 14-60 days), elevating upper-quartile exceedance risk by 33.5% (RR = 1.335; FAR = 0.251).

These findings establish an empirical climatological baseline and highlight the necessity of transparent out-of-sample evaluation in climate risk assessments.

Supplementary information

The online version contains supplementary material, provided as Online Resource 1 (PDF): Supplementary Tables S1-S5 (seasonal data completeness, lag-screening scorecard, soil-

moisture standardization, reanalysis flux conversions and model diagnostics) and Supplementary Fig. S1 (stress-test scenario contrasts).

References

Benjamini Y, Hochberg Y (1995) Controlling the false discovery rate: a practical and powerful approach to multiple testing. J R Stat Soc Ser B 57:289-300. https://doi.org/10.1111/j.2517-6161.1995.tb02031.x

BMD (2019) Operational criteria for heat wave monitoring and early warning protocols. Bangladesh Meteorological Department, Ministry of Defence, Government of the People's Republic of Bangladesh, Dhaka

Brier GW (1950) Verification of forecasts expressed in terms of probability. Mon Weather Rev 78:1-3. https://doi.org/10.1175/1520-0493(1950)078<0001:VOFEIT>2.0.CO;2

Funk C, Peterson P, Landsfeld M, Pedreros D, Verdin J, Shukla S, Husak G, Rowland J, Harrison L, Hoell A, Michaelsen J (2015) The climate hazards infrared precipitation with stations—a new environmental record for monitoring extremes. Sci Data 2:150066. https://doi.org/10.1038/sdata.2015.66

Hersbach H, Bell B, Berrisford P et al (2020) The ERA5 global reanalysis. Q J R Meteorol Soc 146:1999-2049. https://doi.org/10.1002/qj.3803

Huang B, Thorne PW, Banzon VF, Boyer T, Chepurin G, Lawrimore JH, Menne MJ, Smith TM, Vose RS, Zhang H-M (2017) Extended Reconstructed Sea Surface Temperature, version 5 (ERSSTv5): upgrades, validations, and intercomparisons. J Clim 30:8179-8205. https://doi.org/10.1175/JCLI-D-16-0836.1

Hurvich CM, Tsai C-L (1989) Regression and time series model selection in small samples. Biometrika 76:297-307. https://doi.org/10.1093/biomet/76.2.297

Kendall MG (1955) Rank correlation methods, 2nd edn. Charles Griffin, London

Kumar KK, Rajagopalan B, Hoerling M, Bates G, Cane M (2006) Unraveling the mystery of Indian monsoon failure during El Niño. Science 314:115-119. https://doi.org/10.1126/science.1131152

Mann HB (1945) Nonparametric tests against trend. Econometrica 13:245-259. https://doi.org/10.2307/1907187

794 Miralles DG, Teuling AJ, van Heerwaarden CC, Vilà-Guerau de Arellano J (2014) Mega-
795 heatwave temperatures due to combined soil desiccation and atmospheric heat
796 accumulation. Nat Geosci 7:345-349. https://doi.org/10.1038/ngeo2141

797 Muñoz ÁG, Robertson AW (2019) The next generation of sub-seasonal to seasonal climate
798 forecasts: verification, calibration, and decision-support. NOAA Technical Report CPO-
799 8. National Oceanic and Atmospheric Administration, Silver Spring.
800 https://doi.org/10.25923/6n9m-8b36

801 Muñoz-Sabater J, Dutra E, Agustí-Panareda A et al (2021) ERA5-Land: a state-of-the-art
802 global reanalysis dataset for land applications. Earth Syst Sci Data 13:4349-4383.
803 https://doi.org/10.5194/essd-13-4349-2021

804 Nissan H, Burkart K, Coughlan de Perez E, van Aalst M, Mason S (2019) Defining and
805 predicting heatwaves in Bangladesh. J Appl Meteorol Climatol 58:1479-1495.
806 https://doi.org/10.1175/JAMC-D-18-0247.1

807 Pettitt AN (1979) A non-parametric approach to the change-point problem. J R Stat Soc Ser C
808 28:126-135. https://doi.org/10.2307/2346729

809 Rohrer M, Fischer EM, Hortnagl P (2018) Representation of heatwaves and their circulation
810 drivers in reanalysis products. Clim Dyn 53:5377-5396. https://doi.org/10.1007/s00382-
811 018-4458-1

812 Sen PK (1968) Estimates of the regression coefficient based on Kendall's tau. J Am Stat Assoc
813 63:1379-1389. https://doi.org/10.1080/01621459.1968.10480934

814 Seneviratne SI, Corti T, Davin EL, Hirschi M, Jaeger EB, Lehner I, Orlowsky B, Teuling AJ
815 (2010) Investigating soil moisture-climate interactions in a changing climate: a review.
816 Earth-Sci Rev 99:125-161. https://doi.org/10.1016/j.earscirev.2010.02.004

817 Webster PJ, Magaña VO, Palmer TN, Shukla J, Tomas RA, Yanai M, Yasunari T (1998)
818 Monsoons: processes, predictability, and the prospects for prediction. J Geophys Res
819 Oceans 103:14451-14510. https://doi.org/10.1029/97JC02719

820 WMO (2018) Guidelines on the definition and characterization of extreme weather and climate
821 events. WMO-No. 1229. World Meteorological Organization, Geneva

822 **Statements and Declarations**

823 **Funding** This research received no specific grant from any funding agency in the public,
824 commercial, or not-for-profit sectors.

Competing interests The authors have no relevant financial or non-financial interests to disclose.

Author contributions Conceptualization: Fahim Shahriar Pranto; Methodology: Fahim Shahriar Pranto, Abdullah Osama Swaccho; Software: Fahim Shahriar Pranto, Abdullah Osama Swaccho; Formal analysis: Fahim Shahriar Pranto, Abdullah Osama Swaccho; Data curation: Fahim Shahriar Pranto; Investigation: Fahim Shahriar Pranto; Validation: Abdullah Osama Swaccho; Visualization: Fahim Shahriar Pranto; Project administration: Fahim Shahriar Pranto; Supervision: Abdullah Osama Swaccho; Writing - original draft preparation: Fahim Shahriar Pranto; Writing - review and editing: Abdullah Osama Swaccho. Both authors read and approved the final manuscript.

Data availability The daily temperature records for Rajshahi station (BMD Station ID 41923) are not publicly available but can be obtained from the Bangladesh Meteorological Department (https://live3.bmd.gov.bd) on official request for research purposes. The NOAA ERSSTv5 sea surface temperature data are publicly available from the NOAA Physical Sciences Laboratory (https://psl.noaa.gov). The ERA5 and ERA5-Land reanalysis products are available from the Copernicus Climate Change Service Climate Data Store (https://cds.climate.copernicus.eu). The CHIRPS precipitation data are available from the Climate Hazards Center, University of California, Santa Barbara (https://www.chc.ucsb.edu/data/chirps). Processed summary tables supporting this study are provided in Online Resource 1, and the derived heatwave metrics and model outputs generated during the current study are available from the corresponding author on reasonable request.

Code availability The Python code used for heatwave identification, trend analysis, Negative Binomial model fitting, rolling-origin hindcast evaluation and Monte Carlo stress-test simulations is available from the corresponding author on reasonable request and will be deposited in a public repository upon acceptance.

Supplementary Files

This is a list of supplementary files associated with this preprint. Click to download.

- Supplementary.docx